



HAL
open science

Detrital rutile tracks the first appearance of subduction zone low T/P paired metamorphism in the Palaeoproterozoic

Inês Pereira, Craig D Storey, James R Darling, Hugo Moreira, Robin A Strachan, Peter A Cawood

► To cite this version:

Inês Pereira, Craig D Storey, James R Darling, Hugo Moreira, Robin A Strachan, et al.. Detrital rutile tracks the first appearance of subduction zone low T/P paired metamorphism in the Palaeoproterozoic. *Earth and Planetary Science Letters*, 2021, 570, pp.117069. 10.1016/j.epsl.2021.117069 . hal-03284048

HAL Id: hal-03284048

<https://hal.science/hal-03284048>

Submitted on 12 Jul 2021

HAL is a multi-disciplinary open access archive for the deposit and dissemination of scientific research documents, whether they are published or not. The documents may come from teaching and research institutions in France or abroad, or from public or private research centers.

L'archive ouverte pluridisciplinaire **HAL**, est destinée au dépôt et à la diffusion de documents scientifiques de niveau recherche, publiés ou non, émanant des établissements d'enseignement et de recherche français ou étrangers, des laboratoires publics ou privés.

1 Detrital rutile tracks the first appearance of subduction zone low

2 T/P paired metamorphism in the Palaeoproterozoic

3 **Inês Pereira^{1,2*}, Craig D. Storey², James R. Darling², Hugo Moreira^{2,3}, Robin A.**

4 **Strachan², Peter A. Cawood⁴**

5 *¹Université Clermont Auvergne, CNRS, IRD, OPGC, Laboratoire Magmas et*

6 *Volcans, F-63000 Clermont-Ferrand, France, ines.pereira@uca.fr*

7 *²School of the Environment, Geography and Geosciences, University of Portsmouth,*

8 *Portsmouth, PO1 3QL, Hampshire, United Kingdom, craig.storey@port.ac.uk;*

9 *james.darling@port.ac.uk; rob.strachan@port.ac.uk*

10 *³Géosciences Montpellier CNRS, Université de Montpellier, 34090 Montpellier,*

11 *France, hugo.moreira@umontpellier.fr*

12 *⁴School of Earth, Atmosphere and Environment, Monash University, Wellington Rd,*

13 *Clayton VIC 3800, Australia, peter.cawood@monash.edu*

14

15 **ABSTRACT**

16 Earth is unique in the Solar System as the only planet characterised by an active plate

17 tectonic regime. However, there is still no consensus on whether this was fully operational in

18 the Archaean or if it did not develop until the Proterozoic. The metamorphic record offers

19 valuable insight into this debate, since paired, high and low T/P metamorphic conditions are

20 a hallmark of modern plate tectonics. However, much of the metamorphic rock record has

21 either been eroded or overprinted by subsequent tectonothermal events. To address this

22 issue, we examine the detrital rock record and evaluate the potential of rutile, a mineral that

23 forms during subduction and deep-crustal metamorphic processes, as a proxy to track the

24 existence of low T/P and paired metamorphism. At temperatures of 550 °C, rutile is mostly

25 stable at pressures higher than ca. 13 kbar. We use this relationship and the Zr-in-rutile

26 thermometer to determine peak metamorphic temperatures of detrital rutile grains to track

27 the temporal distribution of low T/P metamorphism. We have compiled a dataset of detrital
28 metamorphic rutile from Archaean to Permian age to trace the occurrence of low and high
29 T/P metamorphism through time. The earliest evidence of low T/P from detrital rutile is at
30 about 2.1 Ga. This agrees with the earliest evidence of eclogite facies conditions from the
31 rock record and it also implies that these conditions must have been more prevalent than the
32 present rock record seems to indicate. Together, our study confirms that subduction zone
33 low T/P metamorphism has been fully operating since at least the late Palaeoproterozoic.

34 Keywords: metamorphic proxy; low T/P metamorphism; paired metamorphism; detrital rutile;
35 plate tectonics; Palaeoproterozoic

36 **1. INTRODUCTION**

37 The cyclic formation of supercontinents by modern plate tectonics is of critical importance to
38 the secular evolution of the Earth System. It impacts, for example, the oxygenation of the
39 atmosphere (Campbell and Squire, 2010), nutrient addition to the oceans (Reinhard et al.,
40 2017; Zerkle, 2018), and the geological record itself (Dhuime et al., 2017; Li et al., 2003).
41 Earth experienced major changes between 3 and 2 Ga (Cawood et al., 2018; Condie, 2018;
42 Brown et al., 2020), including variations in the composition of the continental crust (Laurent
43 et al., 2014a), and a change in the rate of continental growth (Dhuime et al., 2012). Several
44 of these changes have been linked to the onset of subduction as a response to the secular
45 cooling of the mantle. However, subduction may have been localized and unstable on the
46 early Earth and therefore may not in itself provide evidence for modern plate tectonics,
47 which requires sustained subduction (Brown et al., 2020; Cawood et al., 2018). It is therefore
48 necessary to investigate the geological record for evidence of the major hallmarks of modern
49 plate tectonics, namely the existence of self-sustained, interlinked subduction systems
50 (Lenardic, 2018).

51 The metamorphic rock record provides strong evidence for sustained subduction for
52 at least the last 700 million years (Brown et al., 2020; Brown and Johnson, 2018; Stern,

53 2005) with the prevalence of low-temperature eclogite and blueschist facies, and paired
54 metamorphism. This record of cold-subduction is widespread in the Phanerozoic (Brown and
55 Johnson, 2018), but the apparent absence of evidence for low geothermal gradients (T/P) in
56 the greater part of the Proterozoic and during the Archaean (Brown et al., 2020; Brown and
57 Johnson, 2018) has been argued as indicating that a different tectonic regime prevailed prior
58 to the Neoproterozoic (Kusky, 2020; Stern, 2005). Exceptionally, late Palaeoproterozoic,
59 partially retrogressed eclogite units have been reported (e.g. François et al., 2018; Ganne et
60 al., 2012; Melnik et al., 2021; Weller and St-Onge, 2017), providing a growing body of
61 evidence for cold-subduction and strong plates that allowed the exhumation of these units.
62 However, due to the rather fragmentary and scarce repository of rocks recording these
63 conditions, the assertion that modern plate tectonics has been fully operating since then has
64 proven contentious. The period between the Palaeoproterozoic and the early Neoproterozoic
65 may be characterized by an intermediate plate tectonic cycle between early Earth and
66 modern-like endmembers (Brown and Johnson, 2018).

67 The identification of certain metamorphic conditions relies on the preservation of
68 indicator minerals; for example, the presence of lawsonite or glaucophane is indicative of HP
69 conditions. However, these hydrous mineral phases are prone to dehydration reactions
70 during retrogression from HP conditions (Skelton et al., 2019; Tsujimori et al., 2006) and
71 therefore pristine blueschist and low- T eclogite are rare even in the modern rock record
72 (Lombardo and Rolfo, 2000; Whitney and Davis, 2006). In this study, we aim to provide a
73 new way of probing the metamorphic record and assessing preservation bias, particularly of
74 low T/P metamorphism, by using detrital rutile.

75 Rutile most commonly occurs after Ti-bearing precursors in intermediate to high
76 pressure metamorphic rocks, particularly the latter (Angiboust and Harlov, 2017; Liou et al.,
77 1998; Zack and Kooijman, 2017). It is also found within upper amphibolite and granulite
78 facies terrains, and associated with either magmatic or lower temperature and pressure
79 settings due to fluid precipitating processes (Carruzzo et al., 2006; Gonçalves et al., 2019;

80 Kotková and Harley, 2010). More rarely, rutile has been described as replacing ilmenite at
81 intermediate grades (480-550 °C) in metapelites (Luvizotto et al., 2009). Alongside its higher
82 stability at high pressures, Zr concentrations in rutile are temperature-dependent (Kohn,
83 2020; Tomkins et al., 2007; Zack et al., 2004a). Together, this makes rutile an ideal
84 candidate to be used as a proxy of low T/P metamorphism. Although rutile can re-equilibrate
85 during retrogression from higher metamorphic conditions, it is more robust than other
86 minerals such as lawsonite and glaucophane that due to their hydrated nature are prone to
87 re-equilibrate more readily. Rutile is also ubiquitous in detrital rocks, and thus it commonly
88 survives weathering and transport. By investigating the sedimentary archive using detrital
89 rutile we expect to be able to develop a more complete picture of the metamorphic record
90 through time, compared with that derived from currently exposed metamorphic terrains
91 (Brown and Johnson, 2019). This approach will allow: 1) tackling the individual metamorphic
92 evolution of Precambrian terranes whose current crustal exposure is from deeper orogenic
93 roots and thus bias the known metamorphic record towards higher-grade conditions, and 2)
94 investigating Earth's long term metamorphic secular evolution, and its tectonic drivers, at a
95 global scale.

96 2. SAMPLES, APPROACH AND METHODS

97 We have investigated published Zr-in-rutile geothermometry data from metamorphic rocks
98 (appendix 1) to evaluate the potential of rutile as a proxy for low T/P metamorphism and
99 some of the limitations associated with this approach. We also looked at detrital rutile
100 datasets reporting U-Pb ages and a complete range of trace element data that are required
101 for source discrimination and geothermometry, that include Cr, Zr, Nb, Sn, Hf, Ta and W.
102 This results in the first combined data compilation of detrital rutile, using data from six
103 published datasets (Agangi et al., 2020; Flowerdew et al., 2019; Rösel et al., 2018, 2014;
104 Şengün et al., 2020; Zhou et al., 2020), from different regions and depositional ages,
105 culminating in a dataset of detrital rutile ages ranging from the Permian to the Archean
106 (appendix 2). To complement this dataset, we collected new trace element data from 161 U-

107 Pb concordant detrital rutile grains, from samples collected in NW Scotland. These
108 correspond to a stratigraphic succession of Neoproterozoic to Cambrian in age: the Torridon
109 Group and the Ardvreck Group, Eriboll Formation. Six samples were prepared from these
110 units (3 from the Torridon Grp. and 3 from the Eriboll Fm.) and rutile grains were handpicked
111 after common mineral separation procedures (see Pereira et al., 2019). Sample locations
112 and U-Pb data for these rutile grains are presented and discussed in Pereira et al. (2020). U-
113 Pb concordant rutile grains were then subjected to trace element analysis using LA-ICPMS.
114 BSE images were used to target the same domains as sampled during the U-Pb isotopic
115 analysis. Rutile grains included in this study are mostly homogeneous, with no apparent
116 BSE (trace element composition) zonation, and yield U-Pb ages ranging from 1.0 to 2.9 Ga.
117 The total dataset comprises 840 analyses (appendix 4).

118 **Trace element microanalysis by Laser ablation coupled inductively plasma Mass**
119 **Spectrometry (LA-ICPMS)**

120 Trace elements in rutile were determined using an ASI RESOLUTION 193nm ArF excimer
121 laser coupled to the ANALYTIK JENA Plasma Quant Elite quadrupole ICP-MS at the
122 University of Portsmouth (UoP). Rutilites were ablated with laser beam diameters between 25
123 and 40 μm , using an energy density of $\approx 4.0 \text{ J/cm}^2$ and a repetition rate of 5 Hz. Analyses
124 consisted of 20 s background, 30 s ablation and sample acquisition, and 5 s of washout,
125 resulting in 55 s per analysis. Instrumental parameters and ablation conditions are
126 summarized in the supplementary file A. The following isotopes were analysed: ^{49}Ti , ^{29}Si ,
127 ^{25}Mg , ^{45}Sc , ^{51}V , ^{52}Cr , ^{87}Sr , ^{89}Y , ^{90}Zr , ^{93}Nb , ^{95}Mo , ^{118}Sn , ^{121}Sb , ^{139}La , ^{140}Ce , ^{141}Pr , ^{146}Nd , ^{147}Sm ,
128 ^{153}Eu , ^{157}Gd , ^{159}Tb , ^{165}Ho , ^{166}Er , ^{169}Tm , ^{172}Yb , ^{175}Lu , ^{177}Hf , ^{181}Ta , ^{182}W , ^{208}Pb , ^{232}Th and ^{238}U .

129 A sample-standard bracketing method was used to correct for instrumental drift using
130 BCR-2 as the reference material (using reported concentrations from Jochum et al. (2005)).
131 R10 (GEOREM database), BHVO (using reported concentrations from Jochum et al. (2005))
132 and NIST610 and 612 (reported concentrations from Jochum et al. (2011)) were used as

133 secondary standards, analysed between unknowns and primary standards in the sample-
134 standard bracketing method. NIST610 and R10 were analysed using a 40 μm laser beam
135 diameter. In contrast, for the BHVO reference material, a laser beam of 80 μm diameter was
136 used to directly access the attenuation mode of the ANALYTIK JENA ICP-MS, important for
137 stable measurement of ^{49}Ti . TiO_2 was used as an internal standard to normalise the intensity
138 of all unknowns, using reference reported values for glasses, and using Ti of 58.8 wt% for all
139 rutile grains). Data were processed using the software package IOLITE 3.31. For Zr, we
140 obtained 5% accuracy relative to published values for all glass standards, within 5% from
141 published values for R10 (GEOREM database) and a 0.06 ppm detection limit. The full
142 instrumental and analytical setup and standard data can be found in appendix 3.

143 3. ZR-IN-RUTILE GEOTHERMOMETRY APPLIED TO DETRITAL GRAINS

144 3.1 Application of the Zr-in-rutile thermometer

145 The Zr-in-rutile thermometer has been calibrated based on natural samples by Zack et al.
146 (2004). Several other researchers have subsequently refined the calibration, including
147 Tomkins et al. (2007) who demonstrated a minor pressure dependency, more significant in
148 the alpha-quartz field. These calibrations have been recently revisited by Kohn (2020) who
149 used new natural data, refined previous natural datasets, and combined them with published
150 experimental data into a new equation that we use in this study. In Figure 1, a comparison
151 between temperature estimates obtained by Zr-in-rutile and mineral equilibria using
152 conventional thermobarometry from 14 published studies (appendix 1) is presented. In most
153 circumstances, thermobarometry based on element exchange between mineral pairs yields
154 a larger uncertainty than single grain thermometers (Fig. 1). Uncertainties in applying this
155 calibration are around 10-15 $^{\circ}\text{C}$, which is often the variation achieved taking into account the
156 uncertainty in the assumed pressure (Fig. 1). On the other side, the standard deviation of Zr
157 concentrations between grains within the same sample propagates into a larger uncertainty
158 that often exceeds that obtained from mineral equilibria (Fig. 1).

159 The linear correlation between both methods is consistent, yielding a ratio not far
160 from 1 (Fig. 1A). This correlation is improved if the temperature estimate used for the
161 correlation taken from mineral equilibria is adjusted to its uncertainty ($R^2 = 0.72$; Fig 1B). For
162 instance, often peak conditions are given as a range, and the true value is enclosed in the
163 interval. Instead of the average, we compare the T estimate determined from Zr-in-rutile and
164 check whether the temperature is enclosed by the interval. If so, the value is taken as the
165 true average T for the correlation. Where this difference is larger than the interval, the
166 uncertainty from the average T estimate from mineral equilibria is either summed or
167 subtracted to obtain the best correlation scenario. In doing so, it becomes clear that for most
168 samples, average Zr concentrations and their uncertainties have a robust fit with the
169 thermobarometric estimate of their rocks, with a tendency line that is essentially 1:1 (Fig.1).

170 Regardless of the calibration equation, rutile has to be in equilibrium with zircon and
171 quartz, so that $t\text{-ZrO}_2$ and $\alpha\text{-quartz}$ activities are 1. As Triebold et al. (2012, 2007)
172 demonstrate, by applying a discrimination diagram based on Cr and Nb (Meinhold et al.,
173 2008; Zack et al., 2004b), rutile grains that have metafelsic affinity can be presumed to have
174 formed in such conditions. Therefore, a filter was applied to enable distinction between
175 probable protolith sources, and thus to infer silica activity in the system. By applying the
176 $\log(\text{Cr}/\text{Nb})$ following Meinhold et al. (2008), grains with $\log(\text{Cr}/\text{Nb}) < 0$ and $\text{Nb} > 800$ ppm
177 were considered as metafelsic and thus yield $a_{\alpha\text{-quartz}} = 1$, whereas grains with $\log(\text{Cr}/\text{Nb}) > 0$
178 or $\text{Nb} < 800$ ppm were considered metamafic and the $\alpha\text{-quartz}$ activity is unknown. While at
179 amphibolite facies conditions this discrimination can sometimes fail (metamafic being
180 classified as metafelsic), we stress that metamafic rocks can have $a_{\alpha\text{-quartz}} = 1$. Felsic rocks
181 commonly yield zircon and therefore we assume that grains classified as metafelsic-derived
182 yield $a_{t\text{-ZrO}_2} = 1$. Therefore, by applying this filter, we have a high level of confidence in the
183 Zr-in-rutile thermometry outputs. The statistically comprehensive dataset compiled from the
184 literature (supplementary file B) shows that only about 10 % of the cases (n total = 764) are
185 false positives (i.e. a metamafic-derived grain being discriminated as metafelsic), and rarely

186 a felsic protolith is discriminated as mafic. It is important to note that from the dataset used
187 to estimate this uncertainty, regardless of protolith composition, quartz was always present
188 ($a_{\alpha\text{-quartz}} = 1$).

189 3.2 Zr concentration scatter and its significance

190 Zr-in-rutile has become a popular tool to retrieve peak temperatures from metamorphic
191 rocks. Several issues have been systematically found from applying this thermometer (Cruz-
192 Uribe et al., 2018; Kooijman et al., 2012; Pape et al., 2016), such as high Zr concentration
193 deviations in grains from the high temperature domain (> 800 °C; Fig. 2). Natural scatter
194 present in most metamorphic rocks, and from the subset we have used (appendix 1), is not
195 commonly observed in eclogite (Fig. 2) or blueschist-facies rocks (Gao et al., 2014; Hart et
196 al., 2016), and when present, it is usually envisaged as recording multiple stages during
197 prograde growth (Spear et al., 2006). This imparts some uncertainty when applying this tool
198 to detrital rutile, as one single estimate can represent either the prograde history or natural
199 scatter by other competing processes (e.g., diffusion, local equilibrium, recrystallisation).

200 While scattering of Zr concentration in rutile is commonly present in rocks at higher
201 metamorphic grade, the scatter is significantly more limited at a lower grade, regardless of
202 protolith composition (Fig. 2). The significant data scatter in high grade rocks (granulite,
203 migmatite) amounts to commonly less than or around 100 °C (including rutile as inclusions in
204 other minerals and matrices), but at lower temperatures it implies an overall standard
205 deviation of $\pm 50\text{-}60$ °C or even less. Importantly, minimum values/outliers of the higher-
206 grade rutile grains are never lower than 600 °C (Fig. 2), suggesting that re-equilibration does
207 not seem to take place below those temperatures.

208 3.3 Temperature estimates, uncertainties, and assumptions

209 In the approach taken here, we have no independent pressure proxies that can assist in
210 further distinguishing metamorphic grade/geothermal gradient (e.g., blueschist vs low-T

211 eclogite, amphibolite vs eclogite, high-T eclogite vs granulite). However, a few important
212 assumptions (e.g., constraints on rutile phase stability, Zr diffusion behaviour), support the
213 identification of rutile grains equilibrated at low T/P (Fig. 3). Because at lower temperatures,
214 rutile is not commonly stable at lower than 10 to 12 kbar (Fig. 3; for all types of rock
215 compositions), this implies that all rutile yielding temperatures lower than 550 °C
216 (intersection of minimum low T/P with the rutile-out boundary; yellow star in Fig. 3) will be a
217 proxy for blueschist facies conditions (and low T/P in general).

218 One of the challenges of utilising Zr concentrations to retrieve peak-T also resides in
219 the thermal histories of the source terranes. Because trace element contents can reset
220 under certain conditions, the potential impact of Zr diffusion during cooling or overprinting
221 during a more recent high temperature event (brown dashed lines, Fig. 3) has been
222 considered in agreement with similar reviews from the literature (e.g., Kohn 2020; Tomkins
223 et al., 2007). For a wide range of cooling rates (0.6 to 75 °C/Ma), rutile (ca. 200 µm) grains
224 can start to re-equilibrate at mid- to upper-amphibolite facies during retrogression (Fig. 3). If
225 the source terranes endured polymetamorphism, it would require about 50 Ma at mid-
226 amphibolite/eclogite facies conditions to re-equilibrate the Zr in rutile, or less than 1 Ma at
227 granulite facies conditions (Fig. 3). Zirconium re-equilibration at lower temperatures would
228 require unrealistic cooling rates or thermal-overprinting durations, which again reinforces the
229 suitability of the 550 °C filter as: a) a conservative approach that will only include low-T, low
230 T/P rutile grains, and b) correspond to a real peak-T estimate under low dT/dP conditions,
231 that has not been affected by either diffusion or recrystallisation processes under any
232 realistic geological conditions.

233 As introduced earlier, only in rare circumstances rutile will form at lower than 10-13
234 kbar for $T < 550$ °C (e.g. Luvizotto et al., 2009). Most frequently these are associated with
235 more uncommon protoliths (MgO-rich or CaO-rich metapelites), to fluid-precipitates, and
236 texturally prone not to survive well weathering (due to small size and aggregate-like texture;

237 Luvizotto et al., 2009). Therefore, any bias resulting from this filter (P of 13 kbar & < 100ppm
238 Zr = 550 °C) strongly resides when pressures were higher and not lower than our
239 assumption for rutile stability. This implies that we exclude potential low T/P rutile grains
240 derived from higher temperature eclogite facies rocks. Also, this results in a mix in the field
241 of “blueschist” between low-T eclogite and blueschist derived grains (grey field, Fig. 3). But
242 by doing so, we increase the interval of confidence in this assessment, as we do not include
243 false positives (such as grains formed at higher T/P conditions). If we were to use a different
244 filter (pink star, Fig. 3), we could inevitably include more eclogite facies-derived grains (low
245 T/P), but we would introduce uncertainty from potential HP amphibolite facies-derived grains
246 (intermediate T/P).

247 A pressure of 13 kbar was applied to all grains in the dataset, and uncertainties on
248 this selected pressure (2 kbar) are propagated in quadrature. We consider Zr measurement
249 uncertainty, the calibration uncertainty, and the weighted mean average of the standard
250 deviation of temperature calculated based on all rutile grains from single metamorphic rocks
251 to calculate the final uncertainty (see below). Together, these should account for both Zr-in-
252 rutile variability in natural rocks, and for the analytical uncertainties. A minimum 10-15 °C
253 uncertainty in the calibration is reported from Kohn (2020), while in the literature there is a
254 discussion of the effects on α -quartz activity in the temperature estimate that can amount to
255 about 50-100 °C (that does not affect the metafelsic-derived grains). On average, the
256 propagated natural variance uncertainty amounts to around 3%. We use this value (natural
257 variance) to propagate uncertainties on each single-grain analysis as follows:

$$258 \quad T_{Zr\ rut} \pm = \sqrt{(natural\ variance)^2 + (Zr\ precision)^2 + (P \pm)^2}$$

259 By applying a 13 kbar pressure to the entire dataset, in order to better estimate the
260 low temperature end, we bias most of the higher Zr concentrations in rutile towards the
261 “amphibolite” facies conditions field (Fig. 3 – following the isopleths from eclogite facies
262 conditions to 13 kbar). For example, a rutile grain that originally formed at 25 kbar containing

263 600 ppm Zr (750 °C), when recalculated at 13 kbar yields a 670 °C estimate and will plot in
264 the intermediate T/P field (Fig. 3). The opposite occurs with low-P granulite rutile grains (<
265 10 kbar, formed under high T/P) when recalculated to 13 kbar. Yet, this P variance is
266 restricted to ca. 5 kbar, and thus it might only account for a small T variation (sometimes
267 enclosed within all the propagated uncertainties; < 30 °C; Fig. 3). Therefore, we do not
268 discuss in any particular detail the variance seen in the high-grade metamorphic realm, as
269 this variance reflects several competing factors, but it does indicate the presence of high-
270 grade rutile and thus of high T/P.

271 4. ASSESSING THE METAMORPHIC RECORD BY UTILISING DETRITAL RUTILE

272 4.1. Detrital rutile grains nature: discriminating sources

273 As mentioned in section 1, rutile can grow after metamorphic reactions, in a wide range of
274 bulk rock compositions, or associated to magmatic and fluid precipitating processes. To
275 retrieve peak-T estimates from the Zr-in-rutile geothermometer, rutile grains were screened
276 to assess the process by which they were formed. High field strength elements (HFSE), Sn
277 and W can be used to distinguish some of these different rutile growth processes (Agangi et
278 al., 2019; Pereira et al., 2019). Some key features of magmatic-related rutile include very
279 high W, Sn, Sb and Nb concentrations (e.g. Meinhold et al., 2010; Agangi et al., 2019) or
280 very high Nb/Ta ratios. Rutile is also known to form in ore mineralisation settings yielding
281 very high Sb/V, Sn, Sb and W. Authigenic rutile and/or rutile related to low-T fluids yields low
282 Nb/Ta ratios, as Ta becomes more compatible with rutile in the presence of aqueous fluids,
283 combined with low Zr/Hf ratios (Pereira et al., 2019). Because published analyses of detrital
284 rutile usually lack full trace element composition reporting, only a small fraction of the
285 available U-Pb detrital rutile data could be included in this work.

286 While trace-element based discrimination diagrams are often sensitive to variations
287 in protolith composition, in Agangi et al. (2019) data come from 8 samples, from 3 different

288 areas ($n_{\text{rut}} = 245$) and are combined with extensive published data, making it a rather
289 comprehensive study. In Pereira et al. (2019), the fluid-related field is based on 3 samples
290 from a single unit ($n_{\text{rut}} = 50$), presented together with data from another study reporting
291 authigenic rutile and combined with published metamorphic rutile data ($n_{\text{tot}} = 453$). These
292 boundaries might be broader than depicted in Figure 4, and future studies might better refine
293 these. Still, by combining these different discriminating diagrams, we preclude, as most as
294 possible, inclusion of low-T and -P rutile, as well as magmatic-related rutile grains.

295 Rutile grains from NW Scotland show no significant zonation or alteration, and they
296 mostly lack inclusions. No inclusions of sulphides or extreme porosity were observed, such
297 as commonly reported in rutile from ore deposit settings (Scott and Radford, 2007; Scott et
298 al., 2011; Agangi et al., 2019; Pereira et al., 2019; appendix 4). Published studies also
299 reported similar textures and included only chemically homogeneous grains. Trace element-
300 based discrimination diagrams were applied to our dataset (Fig. 4). The majority of rutile
301 grains yield Nb/Ta and Zr/Hf values commonly found in metamorphic settings, although a
302 few grains yield very low or high Nb/Ta values (Fig. 4A). Most rutile grains yield Sn and W
303 concentrations below 1000 ppm (Fig. 4B, C) and Sb values under 20 ppm (Fig. 4D). Some
304 published data show Sn/Sb-W values compatible with magmatic-related or Au-mineralised
305 sources. Generally, rutile grains included in this study have low Sb/V (Fig. 4C) suggesting
306 that even when Sn-W are more elevated (Fig. 4B), the rutile grains are of a metamorphic
307 origin (Fig. 4).

308 We excluded grains that plot in the *fluid-related* or *magmatic* fields, which reduced
309 the dataset from 840 to 735 (appendix 2). Therefore, the resulting dataset includes only
310 grains that grew from metamorphic reactions, and thus can be used to infer metamorphic
311 conditions.

312 4.2. Low T/P metamorphic record

313 Each datapoint displayed on Figure 5 has been calculated using Kohn (2020) Zr-in-rutile
314 combined equation and a pressure of 13 kbar, following the discussion in section 3. Despite
315 the natural bias in assuming a given temperature, the uncertainties associated with it
316 (discussed in section 3 and that for high T/P rocks it can amount to an overestimation of 30
317 °C) still allow us to draw conclusions regarding the existence of very high, moderately high
318 or low temperature rutile. Rutile temperature data show periods with a wide range,
319 separated by periods of more uniform growth temperatures (Fig. 5) that correspond to
320 events within the supercontinental cycle (e.g. Brown and Johnson, 2019). Periods showing
321 the widest variations in peak metamorphic temperatures occur between 0.3 and 0.55 Ga, 1.0
322 and 1.2 Ga, and 1.7 and 2.1 Ga, corresponding with periods of supercontinent assembly and
323 collisional orogenesis. A significant number of detrital rutile yield temperatures above 850
324 °C, which despite the method used for its determination, are only compatible with rutile
325 formed at granulite facies conditions. These take place during assembly of the Gondwana-
326 Pangea, Nuna and Kenor supercontinents (Fig. 5).

327 Few rutile grains record peak temperatures lower than 550 °C (n = 31) or than 580 °C
328 (n = 62), and the majority of these low T rutile are Phanerozoic in age (Fig. 5). Although the
329 data offers no insight into the geothermal gradient at any particular time, as they overlap with
330 the different T/P fields from (Brown and Johnson, 2018), we can directly link estimated peak
331 temperatures with the geothermal gradient index (Fig. 5). These wide temperature variations
332 are compatible with those described for paired metamorphic belts (Brown and Johnson,
333 2018), indicating quite different metamorphic grades in rocks of the same age. In the
334 Carboniferous and in the Ediacaran where low and high T/P are known, our dataset shows
335 evidence of low- and high-T rutile (and hence low and high T/P), tying together the
336 metamorphic rock and rutile record, and reinforcing the suitability of this approach in probing
337 earlier periods. From this small detrital rutile dataset, we obtained a few low T rutile grains
338 between 1.0 and 1.2 Ga, and also between 1.7 and 2.2 Ga (Fig. 5). We note that those low
339 T/P rutile grains have the same provenance as some of those derived from higher T/P.

340 Therefore, this new approach and dataset confirm the existence of low T/P and paired
341 metamorphism during the late Palaeoproterozoic and late Mesoproterozoic, during both
342 Nuna and Rodinia assembly, as well as in the Neoproterozoic to Palaeozoic during
343 Gondwana and then Pangea assemblies. The number of cases recording Rodinia assembly
344 are few in comparison to Gondwana-Pangea or Nuna, and they only record
345 tectonometamorphic processes from the Grenville Province on east Laurentia (Pereira et al.,
346 2020). U-Pb and Zr resetting of rutile have been reported in other studies (Zack and
347 Kooijman, 2017) and show that Pb diffuses much faster than Zr. Full resetting of the U-Pb
348 system in rutile in these cases would imply the existence of such conditions prior to the late
349 Palaeoproterozoic. Indeed, a few rutile grains with ages between 2.3 and 2.55 Ga yield
350 temperature estimates between 550 and 580 °C but not lower. No older, Archaean rutile
351 grains selected in this study yield low-T indicative of a low T/P gradient (Fig. 5), but more
352 data are required to confirm this observation.

353 **Preservation Bias of the Exposed Metamorphic Crust and ‘Paired’ Metamorphism**

354 In this new compilation of detrital rutile data, we have probed the sedimentary record in the
355 search for low T/P metamorphism by applying the Zr-in-rutile geothermometer to detrital
356 metamorphic rutile covering most of Earth’s history. We show that both low and high T/P
357 conditions can be inferred since at least 2.1 Ga. The absence of Archaean rutile grains
358 yielding < 550 °C is consistent with the absence of low T/P rocks of this age in the Archaean
359 geological record (Brown and Johnson, 2019). Despite the relatively restricted number of
360 low-T eclogite occurrences of Proterozoic age, our relatively small dataset show that these
361 conditions prevailed. Thus, the lack of preserved blueschists and low-T eclogites prior to the
362 Neoproterozoic represents a preservation bias that can be probably linked to retrogression
363 and overprinting of HP-UHP units at suture zones and to the small stability fields of some
364 indicator minerals (e.g. lawsonite). We argue that metamorphic rutile, preserved as detrital
365 grains in the sedimentary record, can track low and high/intermediate T/P conditions through
366 time. Applied to a given basin and using detrital grains of similar age, it can also provide the

367 missing evidence of paired metamorphic conditions over time, which is envisaged as a
368 hallmark of sustained subduction zones in modern plate tectonics. Our data show that both
369 during Rodinia and Nuna assemblies, rutile grains show this dual low and high T/P and thus
370 that modern plate tectonics has been operating since at least the late Palaeoproterozoic,
371 shaping and conditioning the evolution of the continental crust. Furthermore, the absence of
372 low T/P conditions ($T < 550\text{ }^{\circ}\text{C}$) in the late Archaean, both from the detrital rutile and rock
373 records, suggests that contrasting mechanisms were operating during continental assembly
374 at that time. However, some detrital rutile with late Archaean, early Palaeoproterozoic age
375 yield growth temperatures between 550 and 580 $^{\circ}\text{C}$, many of which are of metamafic affinity.
376 In quartz-absent rocks, Zr will be preferentially taken by rutile, implying that by applying the
377 Zr-in-rutile thermometer calibrated for $a_{\alpha\text{-quartz}} = 1$ we are overestimating the temperature.
378 Since there is no other line of evidence to assist in $a_{\alpha\text{-quartz}}$ estimation at the time of rutile
379 growth, we can not ascertain if these temperatures are overestimated, but it leads to an
380 open possibility that low T/P subduction could have taken place at the end of the Archaean.
381 More detrital rutile data yielding those ages are thus required.

382 **CONCLUSIONS**

383 To investigate metamorphic conditions through time, we have looked at detrital rutile
384 preserved in the sedimentary record as a tracer of past metamorphic conditions. Rutile
385 yielding temperatures lower than 550-580 $^{\circ}\text{C}$ is linked to low T/P conditions, which together
386 with very high temperature detrital rutile and the rock record can be used to infer the
387 presence of paired metamorphic conditions and tectonic processes through time.

388 While the likely transition between early Earth geodynamics and the onset of
389 subduction seems to have been diachronous as recorded on different cratons (Cawood et
390 al., 2018; Laurent et al., 2014), we suggest that it is the youngest evidence of this transition
391 that serves as evidence of a completed switch to modern plate tectonics, with an
392 interconnected plate boundary system operating worldwide.

393 The period between the first onset of subduction between 3.2-3.0 Ga (Cawood et al.,
394 2018; Dhuime et al., 2012) and the last appearance of a TTG to sanukitoid transition
395 culminates at 2.13 Ga (Moreira et al., 2020, 2018). This final transition is marked by the first
396 appearance of low T/P and paired metamorphism, as recorded by detrital rutile, in
397 agreement with a few retro-eclogite occurrences with this age (see Brown et al., 2019 for
398 references, and Holder et al., 2019). This transition is also manifested in the current crustal
399 structure of several Palaeoproterozoic age belts, where recent seismological data is
400 consistent with development of a palaeo-subduction network by ca. 2 Ga (Wan et al., 2020)
401 and also with the oldest preserved linked linear orogenic belts of Eburnean age (Condie,
402 2013). Thus, although the metamorphic rock record is envisaged as supporting a major
403 change in geodynamics at the dawn of the Phanerozoic after a protracted transition (Brown
404 et al., 2020; Brown and Johnson, 2018; Stern, 2005), we contend that the preserved rock
405 record indicates that the onset of modern plate tectonics took place during the late
406 Palaeoproterozoic. By using sedimentary rocks as an archive of the continental crust we
407 have started to contribute towards a more complete overview of the low T/P metamorphic
408 conditions through time and of its forcing mechanisms.

409 **ACKNOWLEDGEMENTS**

410 We would like to thank Geoff Long for amazing technical support during sample preparation
411 and Mike Dunk for assistance during sampling. We thank Michael Brown for his valuable
412 comments on an earlier version of this manuscript. We are also thankful to Matthew Kohn
413 and an anonymous reviewer for their constructive comments during peer-review and Alex
414 Webb for his editorial handling. **Funding:** IP wants to thank the University of Portsmouth for
415 providing a PhD bursary, technical support and for funding all analytical work. HM thanks
416 CNPq - Brazil grant 234610/2014-0. PAC acknowledges support from Australian Research
417 Council grant FL160100168.

418 **REFERENCES CITED**

419 Agangi, A., Plavsa, D., Reddy, S.M., Olierook, H., Kylander-Clark, A., 2020. Compositional
420 modification and trace element decoupling in rutile: Insight from the Capricorn Orogen,
421 Western Australia. *Precambrian Res.* 345, 105772.
422 <https://doi.org/10.1016/j.precamres.2020.105772>

423 Agangi, A., Reddy, S.M., Plavsa, D., Fougereuse, D., Clark, C., Roberts, M., Johnson, T.E.,
424 2019. Antimony in rutile as a pathfinder for orogenic gold deposits. *Ore Geol. Rev.* 106,
425 1–11. <https://doi.org/10.1016/j.oregeorev.2019.01.018>

426 Angiboust, S., Harlov, D., 2017. Ilmenite breakdown and rutile-titanite stability in
427 metagranitoids: Natural observations and experimental results. *Am. Mineral.* 102,
428 1696–1708. <https://doi.org/10.2138/am-2017-6064>

429 Brown, M., Johnson, T., 2019. Time's arrow, time's cycle: Granulite metamorphism and
430 geodynamics. *Mineral. Mag.* 83, 323–338. <https://doi.org/10.1180/mgm.2019.19>

431 Brown, M., Johnson, T., 2018. Secular change in metamorphism and the onset of global
432 plate tectonics. *Am. Mineral.* 103, 181–196. <https://doi.org/10.2138/am-2018-6166>

433 Brown, Michael, Johnson, T., Gardiner, N.J., 2020. Plate Tectonics and the Archean Earth.
434 *Annu. Rev. Earth Planet. Sci.* 48, 1–30. [https://doi.org/10.1146/annurev-earth-081619-](https://doi.org/10.1146/annurev-earth-081619-052705)
435 [052705](https://doi.org/10.1146/annurev-earth-081619-052705)

436 Campbell, I.H., Squire, R.J., 2010. The mountains that triggered the Late Neoproterozoic
437 increase in oxygen: The Second Great Oxidation Event. *Geochim. Cosmochim. Acta*
438 74, 4187–4206. <https://doi.org/10.1016/j.gca.2010.04.064>

439 Carruzzo, S., Clarke, D.B., Pelrine, K.M., MacDonald, M.A., 2006. Texture, composition, and
440 origin of rutile in the South Mountain Batholith, Nova Scotia. *Can. Mineral.* 44, 715–729.
441 <https://doi.org/10.2113/gscanmin.44.3.715>

442 Cawood, P.A., Hawkesworth, C.J., Pisarevsky, S.A., Dhuime, B., Capitanio, F.A., Nebel, O.,

443 2018. Geological archive of the onset of plate tectonics. *Philos. Trans. R. Soc. A Math.*
444 *Phys. Eng. Sci.* 376. <https://doi.org/10.1098/rsta.2017.0405>

445 Condie, K.C., 2013. Preservation and recycling of crust during accretionary and collisional
446 phases of Proterozoic orogens: A bumpy road from Nuna to Rodinia. *Geosciences*,
447 3(2), 240-261. <https://doi.org/10.3390/geosciences3020240>

448 Condie, K.C., 2018. A planet in transition: The onset of plate tectonics on Earth between 3
449 and 2 Ga? *Geosci. Front.* 9, 51–60. <https://doi.org/10.1016/j.gsf.2016.09.001>

450 Cruz-Uribe, A.M., Feineman, M.D., Zack, T., Jacob, D.E., 2018. Assessing trace element
451 (dis)equilibrium and the application of single element thermometers in metamorphic
452 rocks. *Lithos* 314–315, 1–15. <https://doi.org/10.1016/j.lithos.2018.05.007>

453 Dhuime, B., Hawkesworth, C.J., Cawood, P.A., Storey, C.D., 2012. A Change in the
454 Geodynamics of Continental Growth 3 Billion Years Ago. *Science* (80-.). 335, 1334–
455 1337.

456 Dhuime, B., Hawkesworth, C.J., Delavault, H., Cawood, P.A., 2017. Continental growth seen
457 through the sedimentary record. *Sediment. Geol.* 357, 16–32.
458 <https://doi.org/10.1016/j.sedgeo.2017.06.001>

459 Flowerdew, M.J., Fleming, E.J., Morton, A.C., Frei, D., Chew, D.M., Daly, J.S., 2019.
460 Assessing mineral fertility and bias in sedimentary provenance studies: examples from
461 the Barents Shelf. *Geol. Soc. London, Spec. Publ.* SP484.11.
462 <https://doi.org/10.1144/sp484.11>

463 François, C., Debaille, V., Paquette, J.L., Baudet, D., Javaux, E.J., 2018. The earliest
464 evidence for modern-style plate tectonics recorded by HP–LT metamorphism in the
465 Paleoproterozoic of the Democratic Republic of the Congo. *Sci. Rep.* 8, 1–10.
466 <https://doi.org/10.1038/s41598-018-33823-y>

467 Ganne, J., De Andrade, V., Weinberg, R.F., Vidal, O., Dubacq, B., Kagambega, N., Naba,
468 S., Baratoux, L., Jessell, M., Allibon, J., 2012. Modern-style plate subduction preserved
469 in the Palaeoproterozoic West African craton. *Nat. Geosci.* 5, 60–65.
470 <https://doi.org/10.1038/ngeo1321>

471 Gao, X.Y., Zheng, Y.F., Xia, X.P., Chen, Y.X., 2014. U-Pb ages and trace elements of
472 metamorphic rutile from ultrahigh-pressure quartzite in the Sulu orogen. *Geochim.*
473 *Cosmochim. Acta* 143, 87–114. <https://doi.org/10.1016/j.gca.2014.04.032>

474 Gonçalves, G.O., Lana, C., Buick, I.S., Alkmim, F.F., Scholz, R., Queiroga, G., 2019. Twenty
475 million years of post-orogenic fluid production and hydrothermal mineralization across
476 the external Araçuaí orogen and adjacent São Francisco craton, SE Brazil. *Lithos* 342–
477 343, 557–572. <https://doi.org/10.1016/j.lithos.2019.04.022>

478 Hart, E., Storey, C., Bruand, E., Schertl, H.P., Alexander, B.D., 2016. Mineral inclusions in
479 rutile: A novel recorder of HP-UHP metamorphism. *Earth Planet. Sci. Lett.* 446, 137–
480 148. <https://doi.org/10.1016/j.epsl.2016.04.035>

481 Jochum, K.P., Weis, U., Stoll, B., Kuzmin, D., Yang, Q., Raczek, I., Jacob, D.E., Stracke, A.,
482 Birbaum, K., Frick, D.A., Günther, D., Enzweiler, J., 2011. Determination of reference
483 values for NIST SRM 610-617 glasses following ISO guidelines. *Geostand.*
484 *Geoanalytical Res.* 35, 397–429. <https://doi.org/10.1111/j.1751-908X.2011.00120.x>

485 Jochum, K.P., Willbold, M., Raczek, I., Stoll, B., Herwig, K., 2005. Chemical Characterisation
486 of the USGS Reference Glasses and BIR-1G Using EPMA , ID-TIMS , ID-ICP-MS and
487 LA-ICP-MS. *Geostand. Geoanalytical Res.* 29, 285–302. <https://doi.org/10.1111/j.1751-908X.2005.tb00901.x>

489 Kohn, M.J., 2020. A refined zirconium-in-rutile thermometer. *Am. Mineral.* 105, 963–971.

490 Kooijman, E., Smit, M.A., Mezger, K., Berndt, J., 2012. Trace element systematics in

491 granulite facies rutile: Implications for Zr geothermometry and provenance studies. *J.*
492 *Metamorph. Geol.* 30, 397–412. <https://doi.org/10.1111/j.1525-1314.2012.00972.x>

493 Kotková, J., Harley, S.L., 2010. Anatexis during high-pressure crustal metamorphism:
494 Evidence from garnet-whole-rock REE relationships and zircon-rutile Ti-Zr thermometry
495 in leucogranulites from the Bohemian Massif. *J. Petrol.* 51, 1967–2001.
496 <https://doi.org/10.1093/petrology/egq045>

497 Kusky, T., 2020. Plate tectonics in relation to mantle temperatures and metamorphic
498 properties. *Sci. China Earth Sci.* 63, 634–642. <https://doi.org/10.1007/s11430-020->
499 [9597-5](https://doi.org/10.1007/s11430-020-9597-5)

500 Laurent, O., Martin, H., Moyen, J.F., Doucelance, R., 2014a. The diversity and evolution of
501 late-Archean granitoids: Evidence for the onset of “modern-style” plate tectonics
502 between 3.0 and 2.5Ga. *Lithos* 205, 208–235.
503 <https://doi.org/10.1016/j.lithos.2014.06.012>

504 Laurent, O., Martin, H., Moyen, J.F., Doucelance, R., 2014b. The diversity and evolution of
505 late-Archean granitoids: Evidence for the onset of “modern-style” plate tectonics
506 between 3.0 and 2.5 Ga. *Lithos* 205, 208–235.
507 <https://doi.org/10.1016/j.lithos.2014.06.012>

508 Lenardic, A., 2018. The diversity of tectonic modes and thoughts about transitions between
509 them. *Philos. Trans. R. Soc. A Math. Phys. Eng. Sci.* 376.
510 <https://doi.org/10.1098/rsta.2017.0416>

511 Li, X. hua, Wei, G., Shao, L., Liu, Y., Liang, X., Jian, Z., Sun, M., Wang, P., 2003.
512 Geochemical and Nd isotopic variations in sediments of the South China Sea: A
513 response to Cenozoic tectonism in SE Asia. *Earth Planet. Sci. Lett.* 211, 207–220.
514 [https://doi.org/10.1016/S0012-821X\(03\)00229-2](https://doi.org/10.1016/S0012-821X(03)00229-2)

515 Liou, J.G., Zhang, R., Ernst, W.G., Liu, J., McLimans, R., 1998. Mineral parageneses in the
516 Piampaludo eclogitic body, Gruppo di Voltri, western Ligurian Alps. Schweizerische
517 Mineral. und Petrogr. Mitteilungen 78, 317–335.

518 Lombardo, B., Rolfo, F., 2000. Two contrasting eclogite types in the Himalayas: Implications
519 for the Himalayan orogeny. *J. Geodyn.* 30, 37–60. [https://doi.org/10.1016/S0264-](https://doi.org/10.1016/S0264-3707(99)00026-5)
520 [3707\(99\)00026-5](https://doi.org/10.1016/S0264-3707(99)00026-5)

521 Luvizotto, G.L., Zack, T., Triebold, S., Von Eynatten, H., 2009. Rutile occurrence and trace
522 element behavior in medium-grade metasedimentary rocks: Example from the
523 Erzgebirge, Germany. *Mineral. Petrol.* 97, 233–249. [https://doi.org/10.1007/s00710-](https://doi.org/10.1007/s00710-009-0092-z)
524 [009-0092-z](https://doi.org/10.1007/s00710-009-0092-z)

525 Meinhold, G., Anders, B., Kostopoulos, D., Reischmann, T., 2008. Rutile chemistry and
526 thermometry as provenance indicator: An example from Chios Island, Greece.
527 *Sediment. Geol.* 203, 98–111. <https://doi.org/10.1016/j.sedgeo.2007.11.004>

528 Moreira, H., Seixas, L., Storey, C., Fowler, M., Lasalle, S., Stevenson, R., Lana, C., 2018.
529 Evolution of Siderian juvenile crust to Rhyacian high Ba-Sr magmatism in the Mineiro
530 Belt, southern São Francisco Craton. *Geosci. Front.* 9, 977–995.
531 <https://doi.org/10.1016/j.gsf.2018.01.009>

532 Moreira, H., Storey, C., Fowler, M., Seixas, L., Dunlop, J., 2020. Petrogenetic processes at
533 the tipping point of plate tectonics: Hf-O isotope ternary modelling of Earth's last TTG to
534 sanukitoid transition. *Earth Planet. Sci. Lett.* 551, 116558.
535 <https://doi.org/10.1016/j.epsl.2020.116558>

536 Pape, J., Mezger, K., Robyr, M., 2016. A systematic evaluation of the Zr-in-rutile
537 thermometer in ultra-high temperature (UHT) rocks. *Contrib. to Mineral. Petrol.* 171.
538 <https://doi.org/10.1007/s00410-016-1254-8>

539 Pereira, I., Storey, C., Darling, J., Lana, C., Alkmim, A.R., 2019. Two billion years of
540 evolution enclosed in hydrothermal rutile: Recycling of the São Francisco Craton Crust
541 and constraints on gold remobilisation processes. *Gondwana Res.* 68, 69–92.
542 <https://doi.org/10.1016/j.gr.2018.11.008>

543 Pereira, I., Storey, C.D., Strachan, R.A., Bento dos Santos, T., Darling, J.R., 2020. Detrital
544 rutile ages can deduce the tectonic setting of sedimentary basins. *Earth Planet. Sci.*
545 *Lett.* 537, 116193. <https://doi.org/10.1016/j.epsl.2020.116193>

546 Province, B., Shield, F., Melnik, A.E., Skublov, S.G., Rubatto, D., Müller, D., Li, X., Li, Q.,
547 Berezin, A. V, Herwartz, D., Machevariani, M.M., 2021. Garnet and zircon
548 geochronology of the Paleoproterozoic Kuru-Vaara. *Precambrian Res.* 353, 106014.
549 <https://doi.org/10.1016/j.precamres.2020.106014>

550 Reinhard, C.T., Planavsky, N.J., Gill, B.C., Ozaki, K., Robbins, L.J., Lyons, T.W., Fischer,
551 W.W., Wang, C., Cole, D.B., Konhauser, K.O., 2017. Evolution of the global
552 phosphorus cycle. *Nature* 541, 386–389. <https://doi.org/10.1038/nature20772>

553 Rösel, D., Zack, T., Boger, S.D., 2014. LA-ICP-MS U-Pb dating of detrital rutile and zircon
554 from the Reynolds Range: A window into the Palaeoproterozoic tectonosedimentary
555 evolution of the North Australian Craton. *Precambrian Res.* 255, 381–400.
556 <https://doi.org/10.1016/j.precamres.2014.10.006>

557 Rösel, D., Zack, T., Möller, A., 2018. Interpretation and significance of combined trace
558 element and U–Pb isotopic data of detrital rutile: a case study from late Ordovician
559 sedimentary rocks of Saxo-Thuringia, Germany. *Int. J. Earth Sci.* 0, 0.
560 <https://doi.org/10.1007/s00531-018-1643-5>

561 Şengün, F., Zack, T., Dunkl, I., 2020. Provenance of detrital rutiles from the Jurassic
562 sandstones in the Central Sakarya Zone, NW Turkey: U-Pb ages and trace element
563 geochemistry. *Chemie der Erde.* <https://doi.org/10.1016/j.chemer.2020.125667>

564 Skelton, A., Peillod, A., Glodny, J., Klonowska, I., Månbro, C., Lodin, K., Ring, U., 2019.
565 Preservation of high-P rocks coupled to rock composition and the absence of
566 metamorphic fluids. *J. Metamorph. Geol.* 37, 359–381.
567 <https://doi.org/10.1111/jmg.12466>

568 Spear, F.S., Wark, D.A., Cheney, J.T., Schumacher, J.C., Watson, E.B., 2006. Zr-in-rutile
569 thermometry in blueschists from Sifnos, Greece. *Contrib. to Mineral. Petrol.* 152, 375–
570 385. <https://doi.org/10.1007/s00410-006-0113-4>

571 Stern, R.J., 2005. Evidence from ophiolites, blueschists, and ultrahigh-pressure
572 metamorphic terranes that the modern episode of subduction tectonics began in
573 Neoproterozoic time. *Geology* 33, 557–560. <https://doi.org/10.1130/G21365.1>

574 Tomkins, H.S., Powell, R., Ellis, D.J., 2007. The pressure dependence of the zirconium-in-
575 rutile thermometer. *J. Metamorph. Geol.* 25, 703–713. [https://doi.org/10.1111/j.1525-
576 1314.2007.00724.x](https://doi.org/10.1111/j.1525-1314.2007.00724.x)

577 Triebold, S., von Eynatten, H., Luvizotto, G.L., Zack, T., 2007. Deducing source rock
578 lithology from detrital rutile geochemistry: An example from the Erzgebirge, Germany.
579 *Chem. Geol.* 244, 421–436. <https://doi.org/10.1016/j.chemgeo.2007.06.033>

580 Triebold, S., von Eynatten, H., Zack, T., 2012. A recipe for the use of rutile in sedimentary
581 provenance analysis. *Sediment. Geol.* 282, 268–275.
582 <https://doi.org/10.1016/j.sedgeo.2012.09.008>

583 Tsujimori, T., Sisson, V.B., Liou, J.G., Harlow, G.E., Sorensen, S.S., 2006. Very-low-
584 temperature record of the subduction process: A review of worldwide lawsonite
585 eclogites. *Lithos* 92, 609–624. <https://doi.org/10.1016/j.lithos.2006.03.054>

586 Wan, B., Yang, X., Tian, X., Yuan, H., Kirscher, U., Mitchell, R.N., 2020. Seismological
587 evidence for the earliest global subduction network at 2 Ga ago. *Sci. Adv.* 6, eabc5491.

588 <https://doi.org/10.1126/sciadv.abc5491>

589 Weller, O.M., St-Onge, M.R., 2017. Record of modern-style plate tectonics in the
590 Palaeoproterozoic Trans-Hudson orogen. *Nat. Geosci.* 10, 305–311.
591 <https://doi.org/10.1038/ngeo2904>

592 Whitney, D.L., Davis, P.B., 2006. Why is lawsonite eclogite so rare? Metamorphism and
593 preservation of lawsonite eclogite, Sivrihisar, Turkey. *Geology* 34, 473–476.
594 <https://doi.org/10.1130/G22259.1>

595 Zack, T., Kooijman, E., 2017. Petrology and Geochronology of Rutile. *Rev. Mineral.*
596 *Geochemistry* 83, 443–467. <https://doi.org/10.2138/rmg.2017.83.14>

597 Zack, T., Moraes, R., Kronz, A., 2004a. Temperature dependence of Zr in rutile: Empirical
598 calibration of a rutile thermometer. *Contrib. to Mineral. Petrol.* 148, 471–488.
599 <https://doi.org/10.1007/s00410-004-0617-8>

600 Zack, T., von Eynatten, H., Kronz, A., 2004b. Rutile geochemistry and its potential use in
601 quantitative provenance studies. *Sediment. Geol.* 171, 37–58.
602 <https://doi.org/10.1016/j.sedgeo.2004.05.009>

603 Zerkle, A.L., 2018. Biogeodynamics: Bridging the gap between surface and deep Earth
604 processes. *Philos. Trans. R. Soc. A Math. Phys. Eng. Sci.* 376.
605 <https://doi.org/10.1098/rsta.2017.0401>

606 Zhou, G., Fisher, C.M., Luo, Y., Pearson, D.G., Li, L., He, Y., Wu, Y., 2020. A clearer view of
607 crustal evolution: U-Pb, Sm-Nd, and Lu-Hf isotope systematics in five detrital minerals
608 unravel the tectonothermal history of northern China. *GSA Bull.* 1–15.
609 <https://doi.org/10.1130/b35515.1>

610

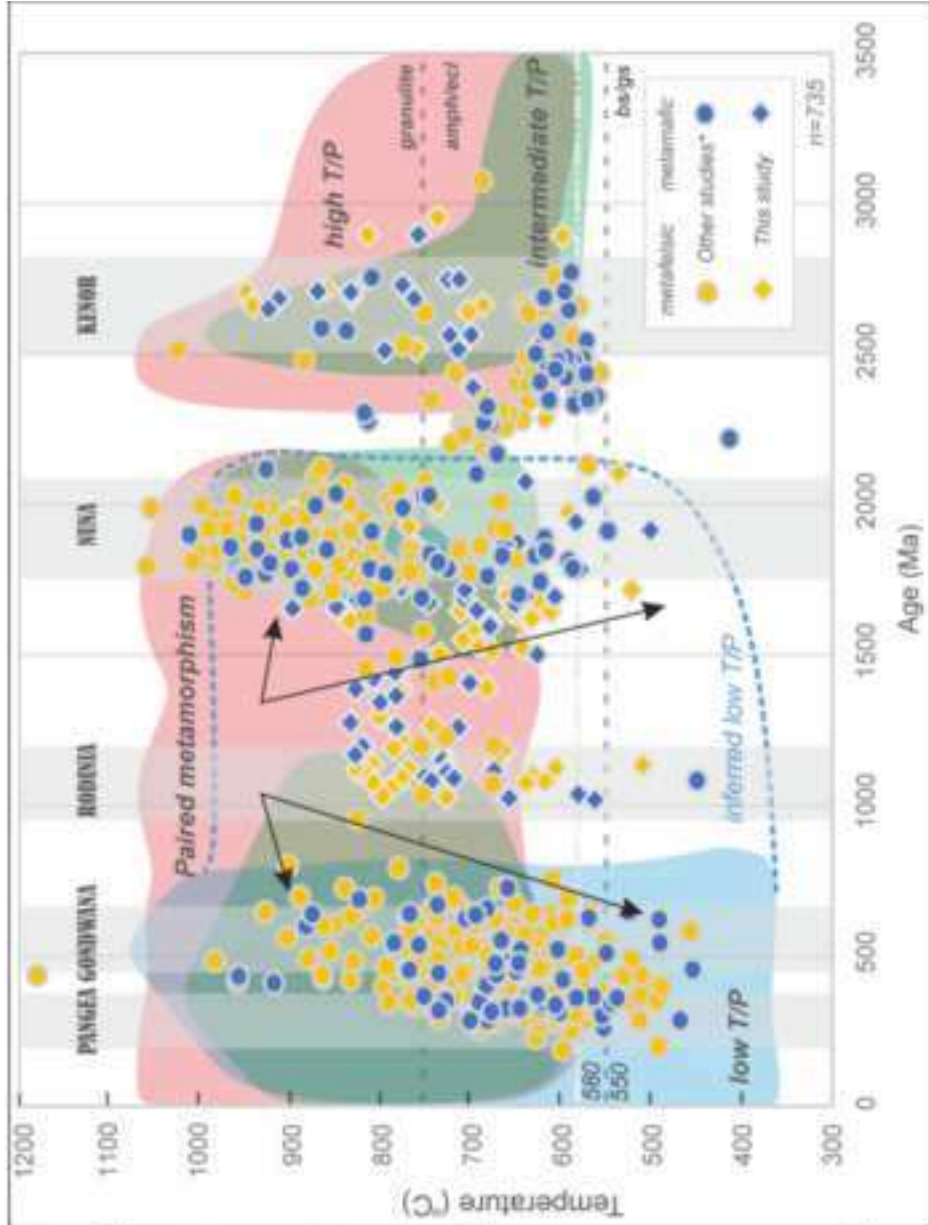
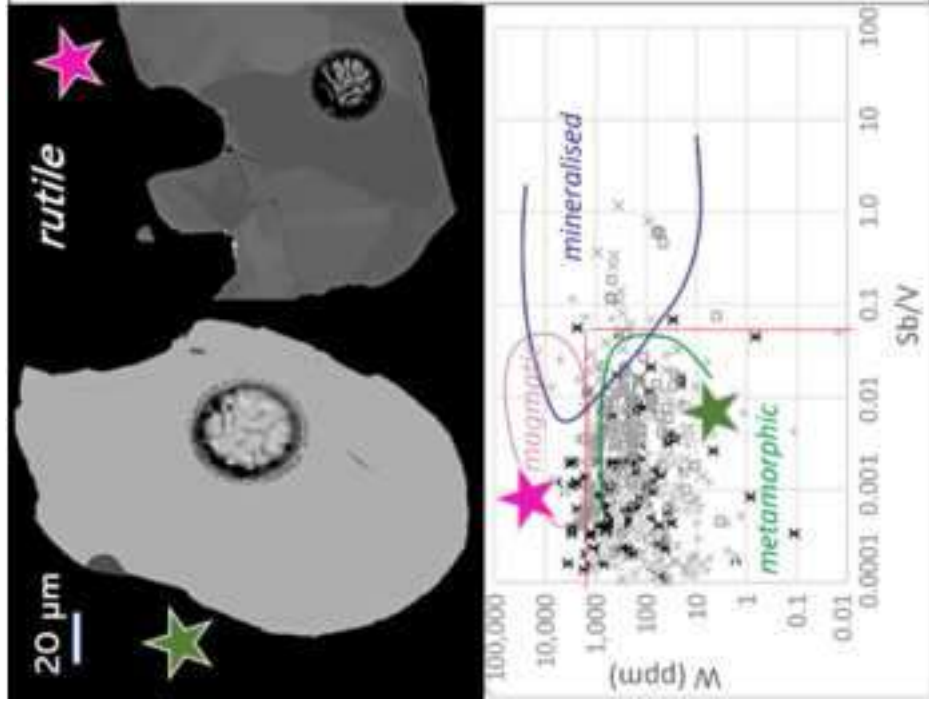


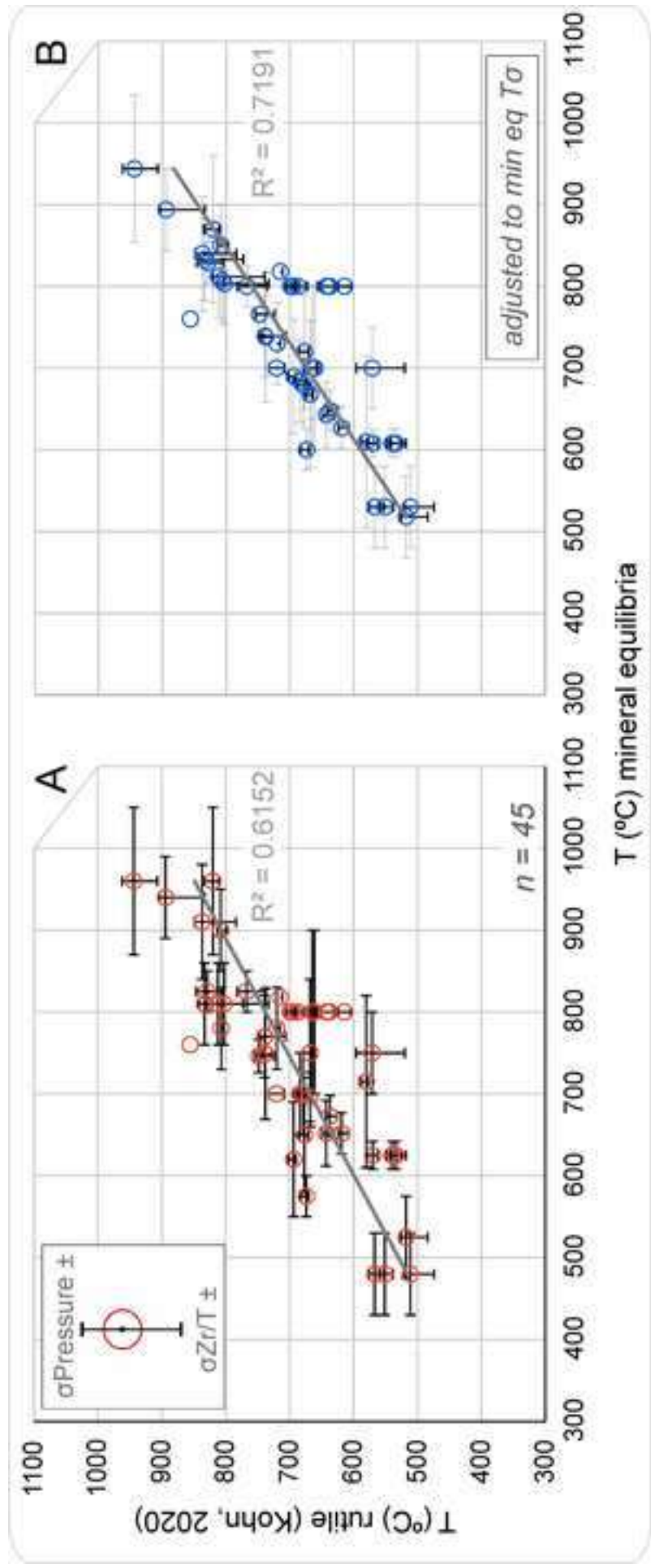
Figure 1. **Comparison between temperature estimates based on Zr-in-rutile (Kohn, 2020) and on mineral equilibria** for 45 samples from 14 published studies (appendix 1). For Zr-in-rutile estimates, average Zr concentrations were used. Uncertainty on the Zr-in-rutile temperatures was calculated using mineral equilibria determined pressure variation and the Zr concentration standard deviation of each sample. A) correlation between both methods using average estimates; B) correlation between both methods adjusting the temperature estimate of mineral equilibria taking into account its variation from classical thermometry.

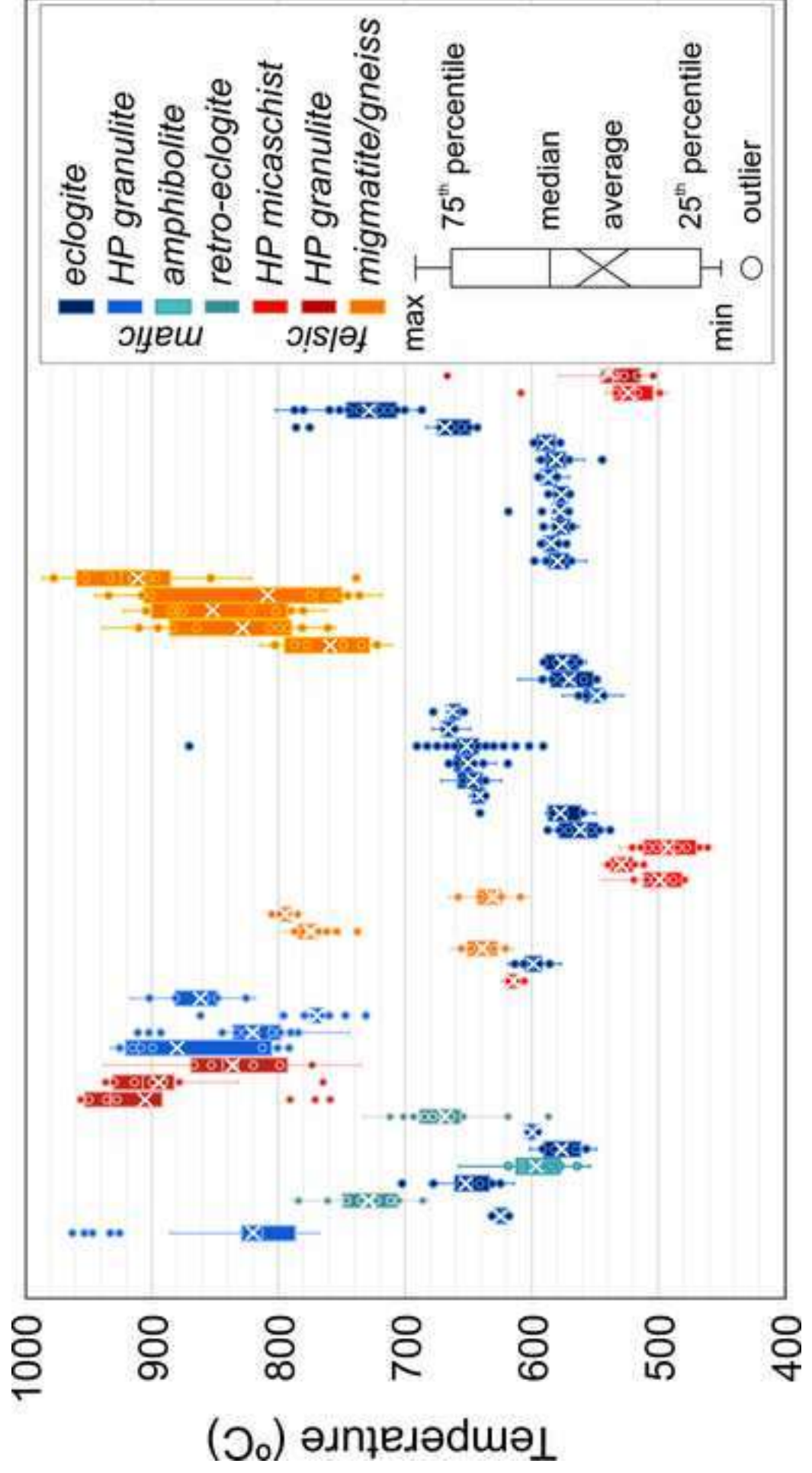
Figure 2. **Boxplot diagram** depicting temperature estimates based on single grain Zr-in-rutile (Kohn, 2020) for multiple samples (n=52), totalling 1123 rutile grains (appendix 1). Each Boxplot corresponds to a different sample, and data are coloured according to different metamorphic grade derived from the mineral assemblage. In cold colours, data derived from metamafic rocks, while warm colours from metafelsic rocks.

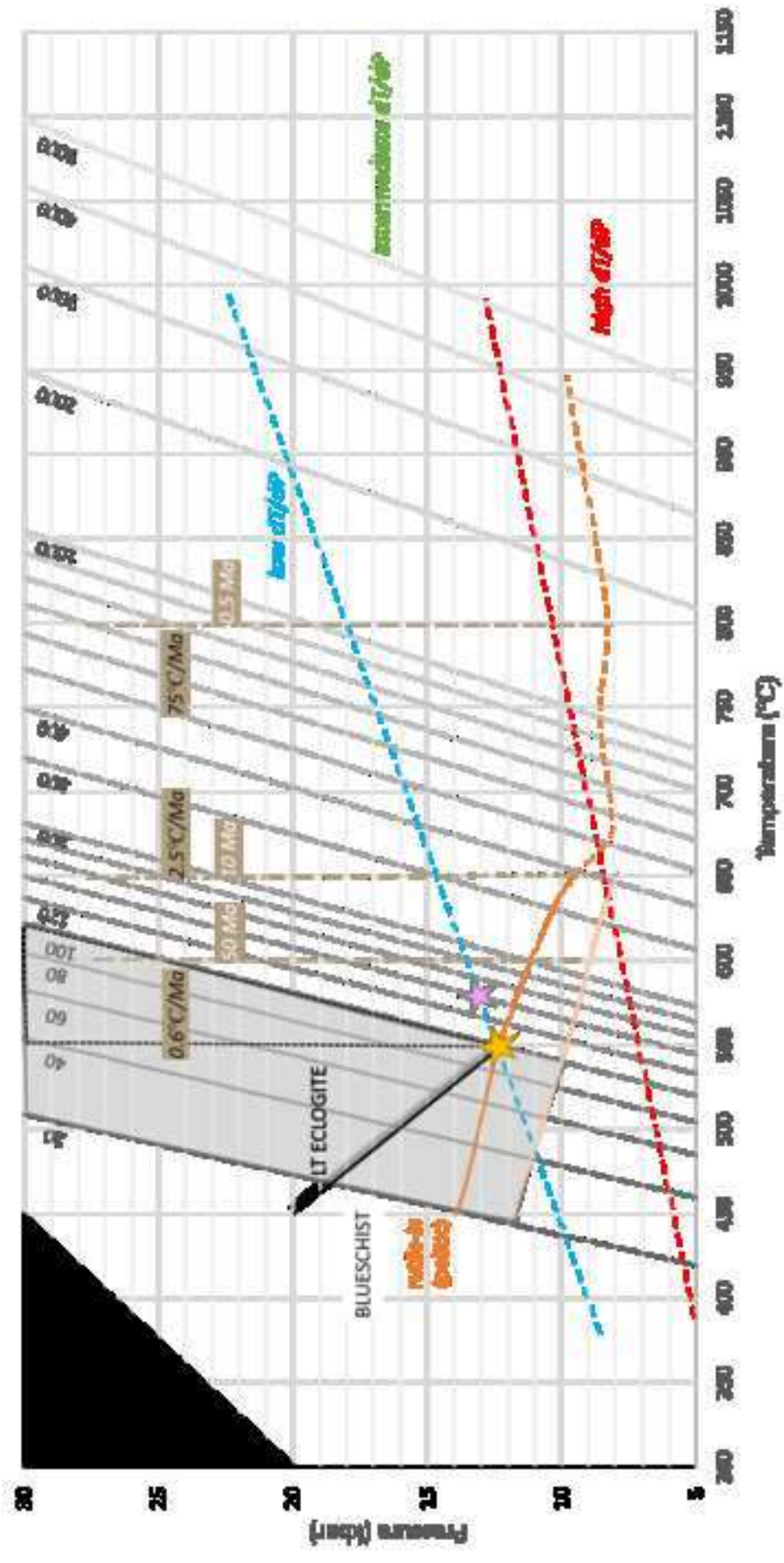
Figure 3. **Temperature-Pressure diagram** for Zr concentrations in rutile (isopleths in grey shades; Kohn 2020). In dashed blue, the minimum conditions for P-T path following low geothermal gradients, and in red, maximum for high geothermal gradients (from Palin et al., 2020). Orange lines correspond to the rutile-in reaction boundary in high silica system (granitoid composition similar to average pelite), the darker line corresponding to the most stable conditions at all given protolith compositions, while light orange to rutile occurrence under low CaO (1 wt%) compositions (from Angiboust and Harlov, 2017). The black line corresponds to the boundary of blueschist to eclogite facies conditions (from Palin et al., 2020). Yellow star corresponds to the intersection of low T/P minimum conditions with the rutile-in reaction and Zr isopleth. This defines for a 100 ppm Zr, at 13 kbar, 550 °C maximum temperature filter. The dashed black triangle highlights the range of conditions that are ignored by applying a temperature filter to the data, which would still be considered low T/P-related conditions. The brown dashed lines correspond to estimates of diffusivity of Zr in rutile (from Cherniak et al., 2007). Each line can be used to interpret the effects of cooling rate or timescales of thermal overprinting-induced diffusion for 200µm grain sizes (which corresponds to the average of observed grain sizes in our samples). Very slow (0.6 °C/Ma), slow (2.5 °C/Ma) or fast (75 °C/Ma) cooling rates of metamorphic terranes can lead to re-equilibration of Zr in rutile to equivalent concentrations of 600 °C, 650 °C or 800°C, respectively. Thermal overprinting events can lead to Zr diffusion if thermal regimes overprint at higher than 600 °C for more than 50Ma, than 650 °C if more than 10 Ma, and to 800°C for over 0.5 Ma. Pink star corresponds to conditions at which rutile could still be assigned as from T/P conditions, but with a lower level of confidence, if we also consider analytical/experimental uncertainties. The black field represents impossible high P, low-T conditions on Earth.

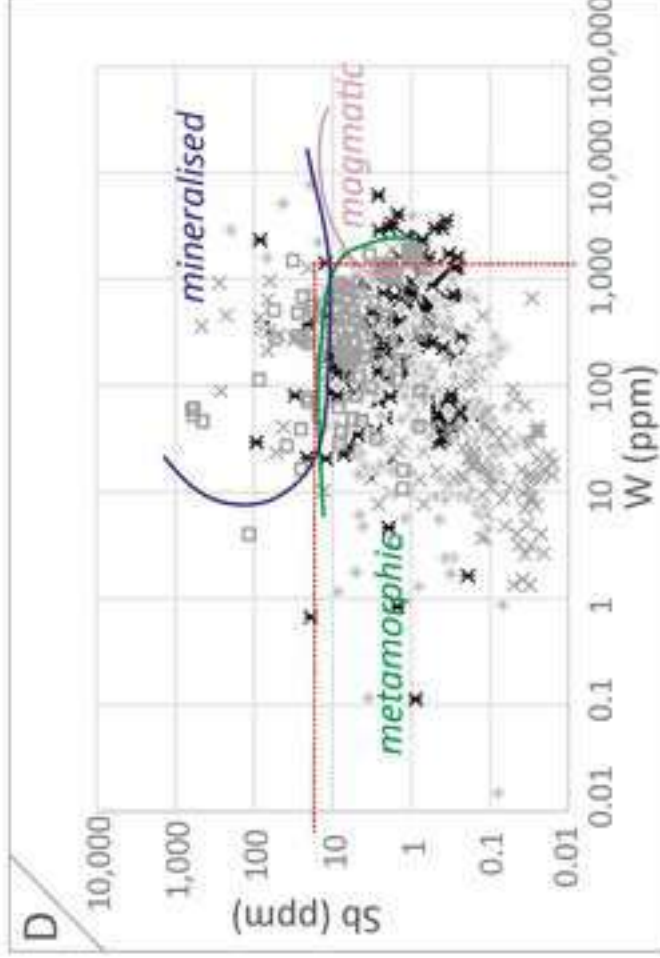
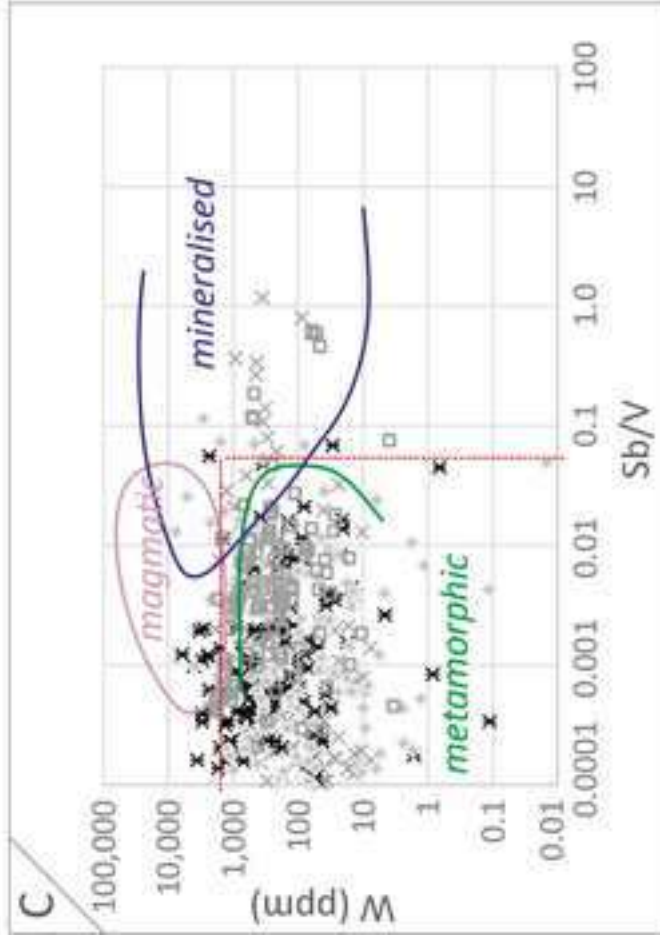
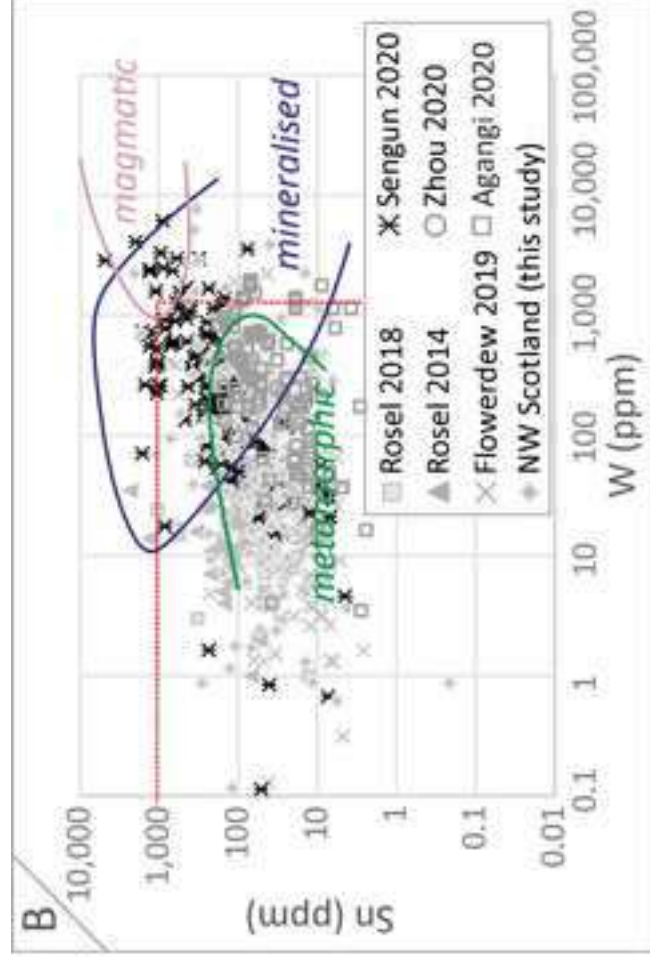
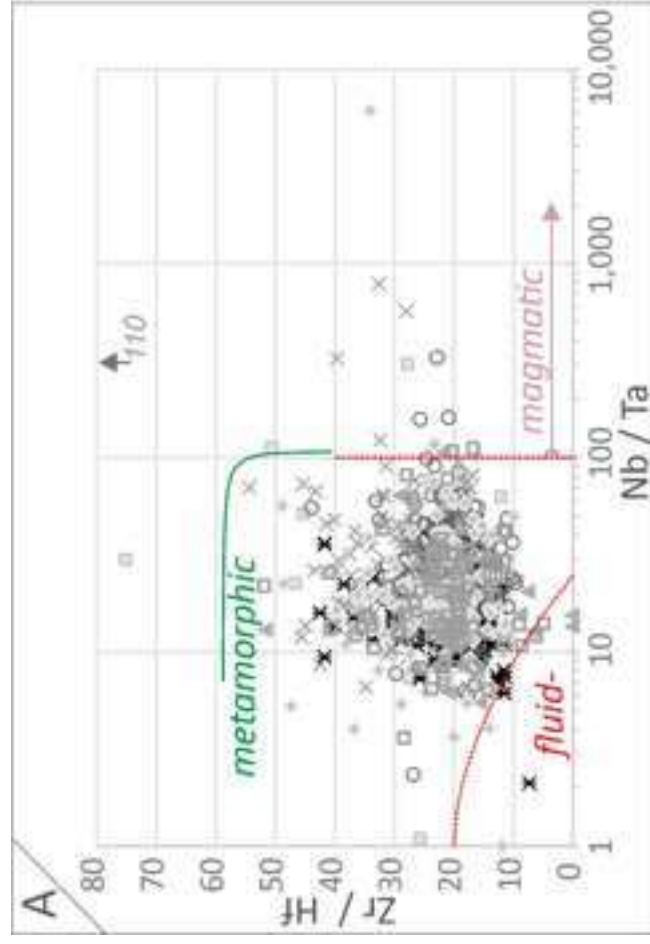
Figure 4. **Discrimination diagrams applied to detrital rutile** (data can be found in appendix 2); **a.** based on Zr/Hf and Nb/Ta from (Pereira et al., 2019) with discriminative fields for low-P fluid-related, metamorphic s.s. and peridotite-related rutile. **b.**, **c.**, and **d.** based on Sn and W, W an Sb/V, and Sb and W concentrations, respectively, from (Agangi et al., 2019) with discriminative fields for metamorphic *sensu stricto*, Au-mineralised related rutile and granitoid-related rutile. Symbols include measurement uncertainties as 1-sigma. Detrital rutile data used in this study to estimate temperatures plot within the metamorphic *sensu stricto* field of both diagrams. Dashed, red lines indicate filters applied for this discrimination.

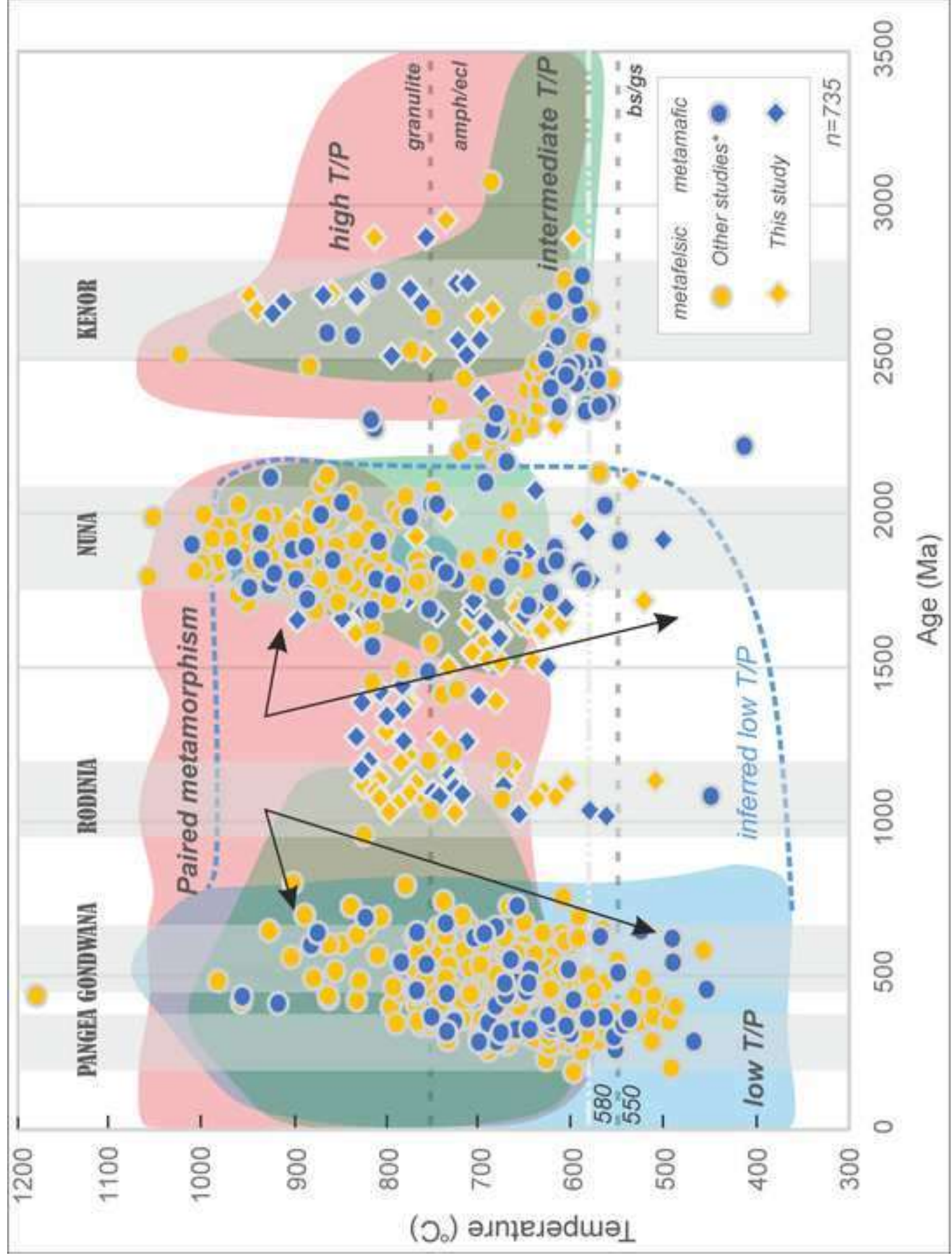
Figure 5. The metamorphic record retrieved from the detrital archive; Metamorphic temperature estimates using the Zr-in-rutile geothermometer at 13 kbar (Kohn, 2020) versus detrital rutile U-Pb age; n = 735. For comparison, fields for low, high and intermediate T/P are plotted from (Brown and Johnson, 2018) and fields dividing temperature ranges for the different metamorphic facies (amph: amphibolite; ecl: eclogite; bs: blueschist; gs: greenschist). Dashed blue line corresponds to the new inferred field for low T/P based on both the detrital rutile and rock record. Yellow symbols correspond to $\log(\text{Cr/Nb}) < 0$ and Nb > 800 ppm (metafelsic; $a_{\alpha\text{-quartz}} = 1$) whereas blue symbols correspond to $\log(\text{Cr/Nb}) > 0$ or Nb < 800 ppm (metamafic; $a_{\alpha\text{-quartz}} = \text{unknown}$) following (Meinhold et al., 2008). Data sources can be found in the text. 1-sigma data uncertainties fall within the symbol used for plotting.

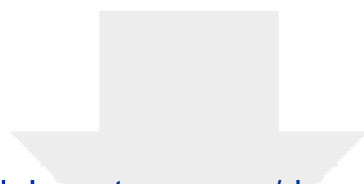








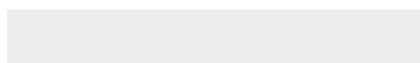
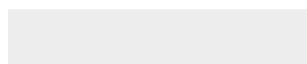


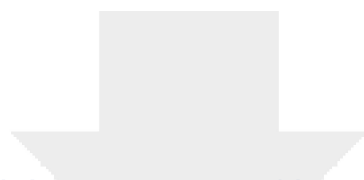


[Click here to access/download](#)

Supplementary material for online publication only

MMC1 - Met rutile Lit.xlsx

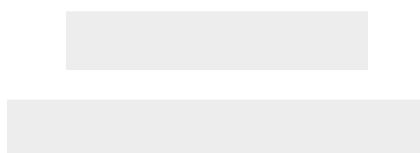


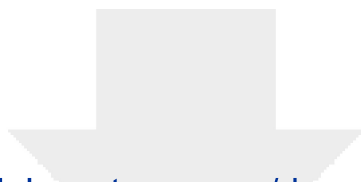


[Click here to access/download](#)

Supplementary material for online publication only

MMC2 - trace and U-Pb detrital rutile.xlsx

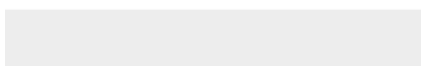
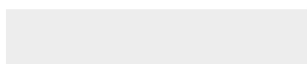


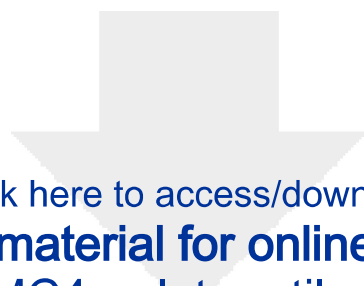


[Click here to access/download](#)

Supplementary material for online publication only

MMC3 - STD Rutile data.xlsx





[Click here to access/download](#)

Supplementary material for online publication only
MMC4 - plate rutile.pdf



Author's contributions: **IP** undertook sample collection and processing, SEM and LA-ICPMS work, data handling and interpretation, and has written the main parts of the manuscript. **CS** supervised the project and data processing, has discussed data interpretation, and substantively revised the manuscript. **JD** provided support during SEM and LA-ICPMS work. **HM** has been involved with data compilation, discussion and manuscript revision. **RS** and **PAC** have provided feedback and discussions related with the background research and have substantively revised the manuscript. All co-authors have contributed to the final version of this manuscript.

Declaration of interests

The authors declare that they have no known competing financial interests or personal relationships that could have appeared to influence the work reported in this paper.

The authors declare the following financial interests/personal relationships which may be considered as potential competing interests: